Development of a momentum vector measurement instrument in steady-state plasmas

Cite as: AIP Advances **8**, 105117 (2018); https://doi.org/10.1063/1.5050553
Submitted: 01 August 2018 . Accepted: 04 October 2018 . Published Online: 15 October 2018

Kazunori Takahashi, Takeharu Sugawara, Hikaru Akahoshi, Yoshinori Takao, and Akira Ando

Development of a momentum vector measurement instrument in steady-state plasmas

Kazunori Takahashi,[1,a] Takeharu Sugawara,[1] Hikaru Akahoshi,[1]
Yoshinori Takao,[2] and Akira Ando[1]
[1]*Department of Electrical Engineering, Tohoku University, Sendai 980-8579, Japan*
[2]*Division of Systems Research, Yokohama National University, Yokohama 240-8501, Japan*

(Received 1 August 2018; accepted 4 October 2018; published online 15 October 2018)

Momentum vector measurement instrument yielding individual and simultaneous identification of local fluxes of momentum components in two different directions, i.e., vector-resolved force, is developed for understanding momentum transport in plasmas and the thrust generation mechanisms of a helicon plasma thruster. A detector plate is attached to a rotational arm connected to a pivot, which has a structure accessible to the inside of the thruster and is mounted on an axially movable balance structure. Simultaneous measurements of displacements of the rotational arm and the axially movable balance give the fluxes of the two different components of the momentum flowing into the detector surface, respectively, e.g., the radial and axial components. The detailed calibration results and the displacement signals induced by applying known forces in a bench test are shown. The results show that the presently developed technique gives resolutions of about 10 μN in the two different directions independently. https://doi.org/10.1063/1.5050553

I. INTRODUCTION

Momentum flux in plasmas, corresponding to a force, is one of the fundamental physical quantities dominating the plasma dynamics as incorporated in a momentum equation, e.g., being used to derive a force imparted by or momentum flux in plasma thrusters.[1–3] The general momentum equation for a charged particle species j (i for ions, e for electrons, and p for plasmas) in steady-state plasmas is given as[4]

$$m_j \nabla \cdot \left(n_j \mathbf{v}_j \mathbf{v}_j \right) = q_j n_j \left(\mathbf{E} + \mathbf{v}_j \times \mathbf{B} \right) - \nabla p_j, \tag{1}$$

where m_j, n_j, $\mathbf{v}_j$, q_j, p_j are the mass, density, velocity, charge, and pressure of particle species j. $\mathbf{E}$ and $\mathbf{B}$ are the electric-field and magnetic-field vectors. Since Eq. (1) corresponds to a local force balance between a Lorentz force and a momentum flux given by sum of the dynamic [left-hand side of Eq. (1)] and static ($p_j = n_j k_B T_j$) pressures, the identification of the momentum flux is essential to understand the plasma fluid dynamics and the local force balance to the fluids, where k_B and T_j are the Boltzmann constant and the temperature.

In typical low temperature laboratory plasmas where the ion temperature is much less than the electron temperature and the electron inertia is negligible, the momentum flux is given by the sum of the electron static and ion dynamic pressures as $n_p k_B T_e + m_i n_p v_i^2$;[1] hence the measurement of the absolute momentum flux requires all the accurate measurements of n_p, T_e, and v_i. In principle these can be carried out by combining some diagnoses such as a Langmuir probe (LP) and a laser-induced fluorescence (LIF). However, it is well known that the measurement of n_p by the LP might include an error in the density estimation, e.g., due to a sheath expansion effect,[5,6] and the T_e in Eq. (1) assume the Maxwellian electron energy distribution, which is rare in low-pressure plasmas

[a]Electronic address: kazunori@ecei.tohoku.ac.jp

as observed in numerous experiments.[7–10] Furthermore, the measurement of the velocity vectors requires a complicated system such as the high-resolution and accurate LIF technique.[11–13] Therefore, the absolute measurement of the momentum flux vector is indeed difficult and requires great effort.

In the field of electric propulsion, a force exerted to a propulsion device is directly measured by attaching it to a pendulum called a thrust balance.[14–17] The thrust force can also be estimated by a pendulum target located in the plasma plume.[18–20] Since the thrust force is equal in magnitude and opposite in direction to the momentum flux ejected from the device, the measurement of the force is indeed equivalent to the identification of the momentum flux. Some of analytical studies on an advanced thruster called a helicon plasma thruster (HPT), which consists of a helicon source and a magnetic nozzle, describes that the thrust force can be given by the sum of a pressure force (T_s) exerted on a back wall terminating the plasma upstream, an axial force (T_w) exerted on a radial wall, and a Lorentz force (T_B) exerted on the magnetic field due to a plasma-induced electric current.[4] By attaching one any of the three structures to the pendulum force balance, the absolute axial force exerted to the structures have been individually identified.[21–23] This approach has demonstrated the momentum transport and conversion processes in the thruster, e.g., the loss of the axial momentum to the radial wall (T_w) and the thrust generation by the magnetic nozzle (T_B), where the momentums integrated over the surface area and over the volume have been obtained, respectively.

Figure 1 shows that the physical picture of the ion behavior near the physical boundary proposed previously,[23] where the contour color shows the measured electron pressure.[24] The previous individual measurement of T_w integrated over the wall has implies that the axial momentum is transferred to the radial wall by the ions accelerated axially in the plasma core (upper inset in Fig. 1) and lost to the radial wall (lower inset in Fig. 1),[23] where the axial electric field in the plasma core is induced by a density gradient concomitantly occurring with a neutral depletion.[25–30] The spatially resolved measurement of the flux of the axial momentum lost to the wall would be useful for further understanding of the momentum transfer mechanisms. Near the radial wall, the ions are accelerated radially by a radial electric field of a sheath and significant plasma energy is expected to be lost to the wall as shown in the previous analysis;[31] hence the measurements of the fluxes of both the radial and axial momentums to the radial wall will give new insights into the plasma dynamics and the thruster development. Since the role of the magnetic nozzle downstream of the thruster is a momentum conversion from a radial momentum to an axial one according to the previous interpretation,[1,10] the simultaneous and vector-resolved measurement of the momentum fluxes is also useful for further understanding of the magnetic nozzle physics. Some types of the vector-resolved force sensors have been developed so far to characterize a plasma plume of a hall effect thruster and a sputtering device.[32–34] However the spatially-resolved and vector-resolved measurement of the local momentum flux cannot be performed by the existing force measurement techniques in Refs. 32–34 due to the poor resolution of the

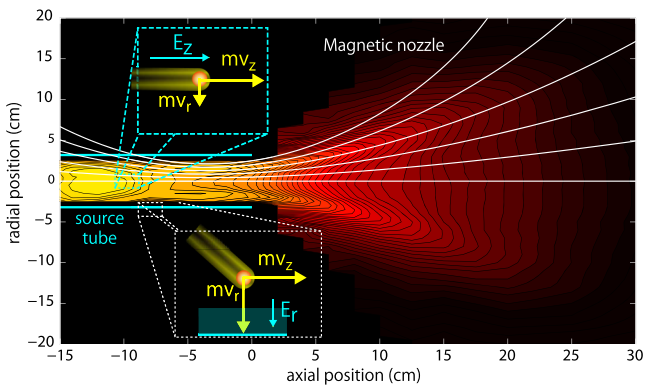

FIG. 1. Schematic of the typical helicon plasma thruster configuration, together with the measured electron pressure (contour color) and the magnetic field lines (solid lines). The axial ion acceleration in the plasma core (upper inset) and the loss of the ion having the radial and axial velocities to the wall (lower inset) are sketched.

balance and/or the absence of the structure allowing their access to the inside of the plasma source. Here a momentum vector measurement instruments providing two different vector components of the momentum flux is developed, where a small target plate is attached to a 3-mm-diameter arm supported by a rotational pivot, which is further mounted on the axially movable balance. The structure allows to insert the detector plate into the source tube of the helicon thruster. The results of the bench test are presented here and the surface area of the detector required for the application to the helicon plasma thruster diagnosis is discussed.

II. EXPERIMENTAL SETUP

Figure 2 shows the schematic diagram of the momentum vector measurement instruments (MVMI), being developed presently. Momentum detector made of a thin insulator mica plate can be attached to an arm as in Fig. 2. It should be mentioned that the target material is same as the previous experiments showing the comparison of the force exerted to the large target plate downstream of the helicon thruster and the directly measured thrust by the pendulum thrust balance, where these two forces are in good agreement.[35] Although the accuracy of the force measurement to the target plate is still in argument due to many effects including the target material sputtering, the previous experiment has implies the negligible sputtering effect on the force measurement in the helicon thruster, where the ion energy entering the target seems to be lower than the other types of the thruster. Let us consider the detector surface facing radially for example (as shown in Fig. 2), yielding the spatially-resolved measurement of the momentum flux to the radial source wall by its axial scan. When the detector surface is exposed to the plasma and the opposite surface is shielded from the plasma, the sheath structure is spontaneously formed in front of the surface, resulting in reflection of the most electrons and the ion acceleration normal to the detector surface, where it should be mentioned that the total momentum flux including both the electrons and ions has to be conserved in the sheath because of the absence of an external energy source as theoretically shown previously.[1] Considering the radial Bohm flux $n_s u_B$ and the loss of the ions having radial and axial velocities (u_r and u_z) at the detector

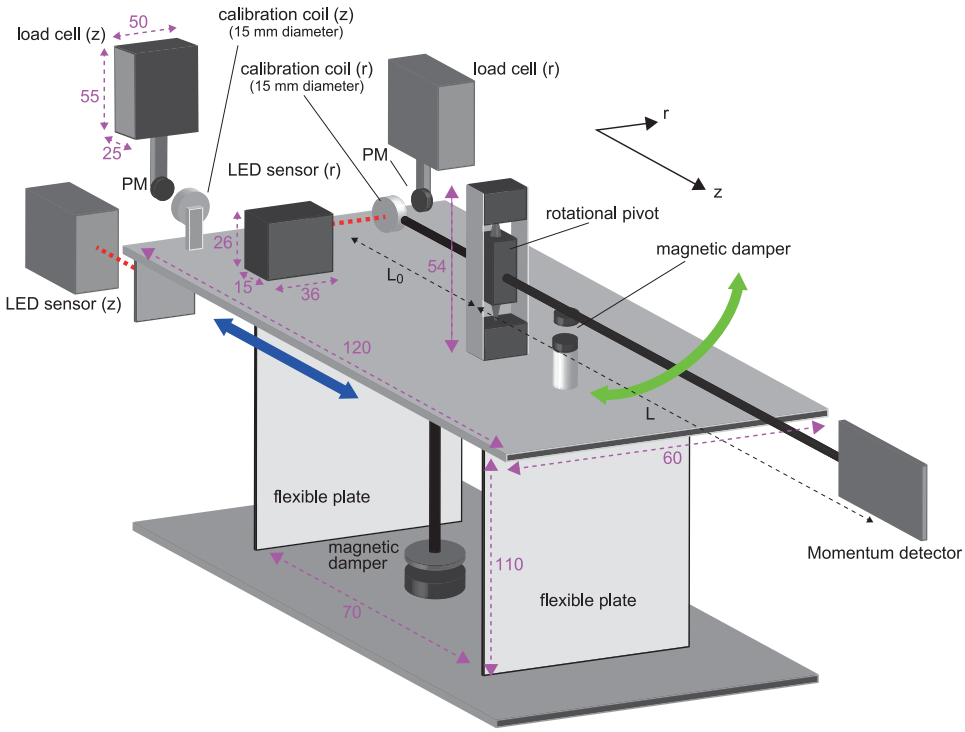

FIG. 2. Schematic of the momentum vector measurement instruments. The representative sizes of the components are indicated in units of mm. The lengths of the two arms are chosen as L_0 = 80 mm and L = 375 mm in the present bench test.

surface, the fluxes of the radial and axial momentums M_{dotr} and M_{dotz} imparted to the radially facing detector surface, which are equivalent to the radial and axial force densities acting to the radially facing detector surface, can be given by

$$M_{dotr} = n_s u_B m_i u_r, \tag{2}$$

$$M_{dotz} = n_s u_B m_i u_z, \tag{3}$$

where n_s, u_B, M_{dotr}, M_{dotz} are the sheath edge density, the Bohm velocity, the flux of the radial momentum, and the flux of the axial momentum to the wall, respectively. The non-negligible flux of the axial momentum integrated over the inner surface area of the helicon source has actually been measured in the previous study.[23] The presently developed MVMI is designed to solely and simultaneously measure these two components, where the whole structure of Fig. 2 except for the detector surface has to be mechanically shielded from the plasma (not shown in Fig. 2) in the future experiment of the plasma thruster. Once again, the fluxes of the momentums in Eqs. (2) and (3) correspond to the radial and axial forces exerted on the radially facing detector surface, respectively. It should be mentioned that setting the detector facing axially on the arm instead of the radially facing detector will give the axial fluxes of the radial and axial momentums to the detector surface, i.e., the radial and axial forces exerted on the axially facing detector surface.

The stainless-steel arm (length L) having the detector and the second arm (length L_0) pointing to the opposite direction to the detector are connected to a rotational pivot supported by a double-needle structure, which can allow them to move only in the rotational direction. When imparting the radial force [Eq. (2)] to the detector, the arm is rotated; the displacement measured by a light-emitting-diode (LED) displacement sensor gives the radial force by multiplying a calibration coefficient relating the displacement to the force. To have a stable initial position of the arm, permanent magnets (PMs) are attached to both the arm and to the stage (magnetic damper). The whole structure including the LED sensor and the rotational pivot is mounted on the stage, which is supported by two flexible plates as in Fig. 2. This structure can allow the stage to move only in the axial direction, where the magnetic damper is installed at the bottom side of the stage. The axial displacement measured by the other LED sensor gives the axial force imparted to the detector by using the other calibration coefficient. If the displacements in the radial and axial directions are individual and induced by only the radial and axial forces respectively, the radial and axial forces corresponding to the momentum flux in Eqs. (2) and (3) can be simultaneously and individually obtained.

In order to have the radial and axial calibration coefficients, radial and axial calibration coils are mounted on the second arm and the axially movable stage as seen in Fig. 2, respectively. Very close to the coils, small PMs connected to a sensitive load cells are located; supplying electric currents I_{calr} and I_{calz} to these calibration coils induces forces between the coil and the PM as utilized previously,[35] where the force to the coil is equal in magnitude and opposite in direction to the force exerted to the PM according to action-reaction law. Hence the magnitudes of the forces exerted to the calibration coils can be obtained by measuring the voltage signals from the load cells, where the signals are digitized by a 16-bit data acquisition system via a precise isolation amplifier having a gain of a thousand. By simultaneously measuring the output voltage (gained by a factor of ten in the present experiment) from the LED sensor, the calibration coefficients relating the radial/axial forces to the radial/axial displacement signals can be obtained.

III. EXPERIMENTAL RESULTS

Bench tests are performed here to demonstrate the concept of the MVMI providing the vector-resolved measurement of the momentum flux. The electric current I_{calr} and I_{calz} are temporally swept from about -0.3 A to + 0.3 A for about 20 sec (t = 10 - 30 sec) as shown in Figs. 3(a) and 4(a); then the radial and axial forces imparted to the PMs attached to the load cells and the output signals V_r and V_z from the LED sensors are measured as shown in Figs. 3(b-c) and 4(b-c), respectively. All the signals linearly changes when sweeping the currents I_{calr} and I_{calz}. The data for t = 10 - 30 sec are extracted from Figs. 3(a-c) and 4(a-c) and plotted in Figs. 3(d-e) and 4(d-e) by dots, respectively, providing the calibration curves relating the forces (F_r and F_z) to the calibration coil current (I_{calr} and I_{calz}) [Figs. 3(d) and 4(d)] and relating the sensor signals (V_r and V_z) to the forces (F_r and F_z)

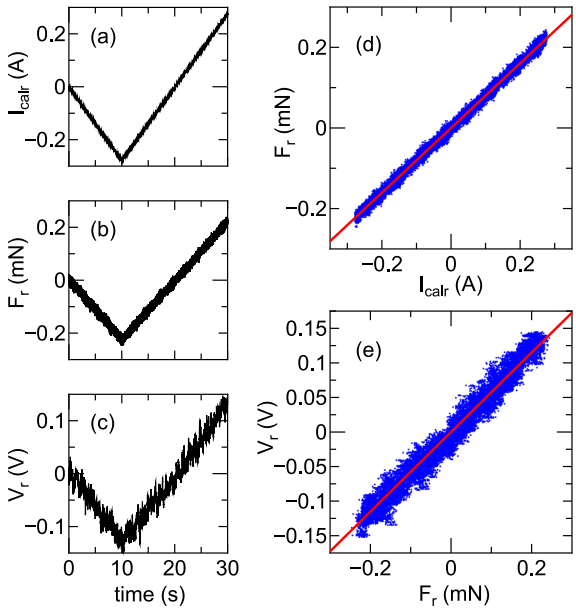

FIG. 3. Temporal variations of (a) the calibration coil current I_{calr}, (b) the force F_r measured by the load cell (r), and (c) the sensor signal V_r from the radial LED sensor. (d) F_r versus I_{calr} and (e) V_r versus F_r extracted from the data for $t = 10 - 30$ sec in (a-c), together with the fitting lines (bold lines) obtained via the least squares method.

[Figs. 3(e) and 4(e)]. These data are found to show the clear linear relations; being fitted by linear lines as shown by the bold red lines, which are obtained by the least squares method. By averaging the fitting coefficients obtained from the fifteen data sets taken for the same conditions, the calibration coefficients can be obtained as

$$F_r = (0.78 \pm 0.03) I_{calr}, \tag{4}$$

$$F_z = (2.98 \pm 0.09) I_{calz}, \tag{5}$$

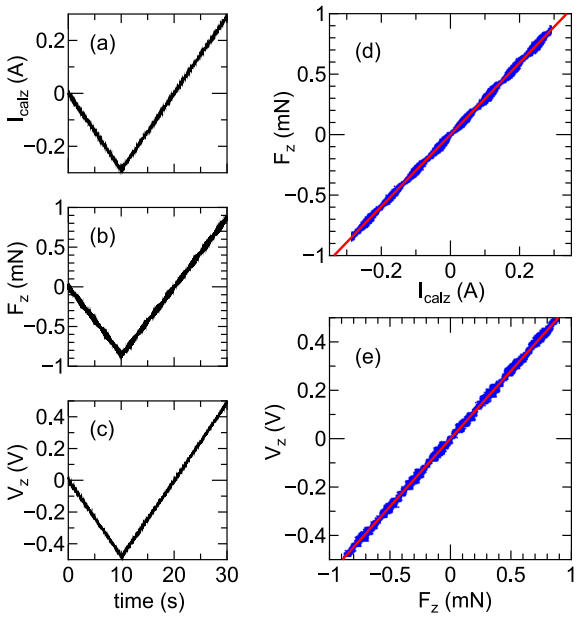

FIG. 4. Temporal variations of (a) the calibration coil current I_{calz}, (b) the force F_z measured by the load cell (z), and (c) the sensor signal V_z from the axial LED sensor. (d) F_z versus I_{calz} and (e) V_z versus F_z extracted from the data for $t = 10 - 30$ sec in (a-c), together with the fitting lines (bold lines) obtained via the least squares method.

$$V_r = (0.59 \pm 0.02)F_r, \tag{6}$$

$$V_z = (0.57 \pm 0.02)F_z, \tag{7}$$

where F, I, and V are in units of mN, A, and V, respectively.

To verify the vector-resolved measurement of the momentum fluxes [Eqs. (2) and (3)], the sensor signals V_r and V_z are simultaneously measured as shown in Fig. 5. When imparting either the radial force (F_r) or the axial one (F_z) by utilizing the calibration coils as in Fig. 5(a) or Fig. 5(b), the other coil current is maintained at zero. It is found that negligible change of the axial displacement signal V_z is detected when imparting only the radial force [Fig. 5(a)], and vice versa [Fig. 5(b)]. These data clearly demonstrate the vector-resolved measurement of the momentum fluxes.

In order to evaluate the cross talk between the radial and axial force measurements, the cross talk coefficient (C_{r-z}) relating the detected axial force to the applied radial force, and vice versa (C_{z-r}), are defined as

$$C_{r-z} = F_{z\ detected}/F_{r\ applied}, \tag{8}$$

$$C_{z-r} = F_{r\ detected}/F_{z\ applied}. \tag{9}$$

The V_r and V_z data for $t = 12 - 20$ sec are extracted from Figs. 5(a) and 5(b), and fitted by a linear line as indicated by the bold dotted lines. The ratio of the slopes of the fitting lines in Figs. 5(a) and 5(b) can give the values of C_{r-z} and C_{z-r}, respectively, where the calibration coefficients in Eqs. (6) and (7) are taken into account. The obtained values of the cross talk coefficients are $C_{r-z} \sim 2.9 \times 10^{-2}$ ~ -30 dB for Fig. 5(a) and $C_{z-r} \sim 8.1 \times 10^{-4}$ ~ -62 dB for Fig. 5(b), respectively. This quantitatively shows the negligible cross talk effect between the radial and axial force measurements.

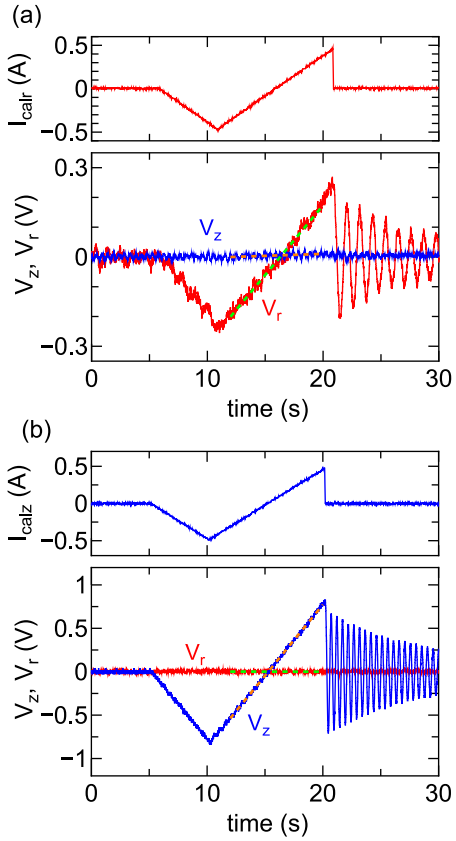

FIG. 5. Temporal variation of the calibration coil currents (a) I_{calr} and (b) I_{calz}, and the simultaneously measured sensor signals V_r and V_z. When sweeping the (a) radial (I_{calr}) or (b) axial (I_{calz}) coil current, the other coil current is maintained at zero. The bold dotted lines overwritten on the V_r and V_z signals are the fitting lines of the data for t = 12-20 sec.

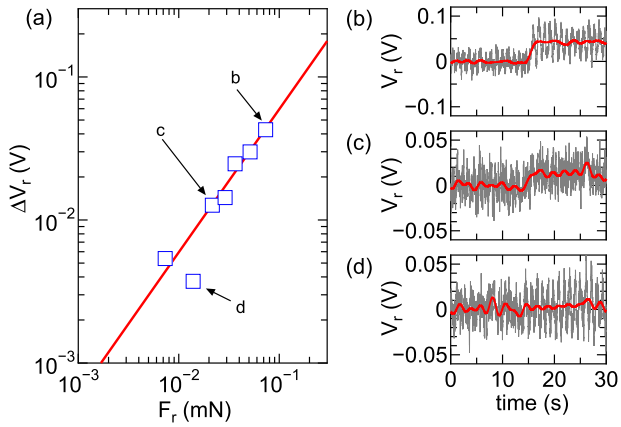

FIG. 6. (a) The radial displacement signal ΔV_r induced by turning on the dc calibration coil current I_{calr} as a function of the imparted force F_r, together with the calibration curve obtained from Fig. 3 and given by Eq. (6). The data obtained from (b-d) are labeled as 'b', 'c', and 'd', respectively. (b-d) Typical raw (thin lines) and filtered (bold lines) radial sensor signal V_r when turning on the dc current I_{calr} to the calibration coil, imparting the continuous radial forces of (b) ~ 73 μN, (c) ~ 21 μN, and (d) ~ 14 μN for $t > 15$ sec.

When measuring the momentum flux transferred to the small detector surface in the rf plasmas, the radial and axial forces to the surface are expected to be very small, being close to a few tens of μN as discussed later. Here lower limits of the radial and axial force detections are investigated by turning on a dc calibration coil currents and measuring the displacements, where the imparted force can be obtained from the supplied coil current via Eqs. (4) and (5) for the radial and axial forces, respectively. From the equilibrium values of V_r or V_z before and after turning on the coil currents at $t = 15$ sec as seen in Figs. 6(b-d) and 7(b-d), the displacement signals ΔV_r and ΔV_r induced by the imparted force can be obtained. The raw and filtered sensor signals are shown by the gray thin and bold red lines, respectively, and the equilibrium values are obtained by numerically averaging the filtered signals for $t = 0 - 10$ sec and $t = 20 - 30$ sec.

Figure 6(a) and 7(a) show the measured displacement signals ΔV_r and ΔV_z (open squares) as functions of the imparted forces F_r and F_z together with the calibration curves (solid lines) given by Eqs. (6) and (7), respectively. The measured data agree well with the calibration curve for the force values larger than 20 μN for the radial direction [Fig. 6(a)] and for all the range of the force for the

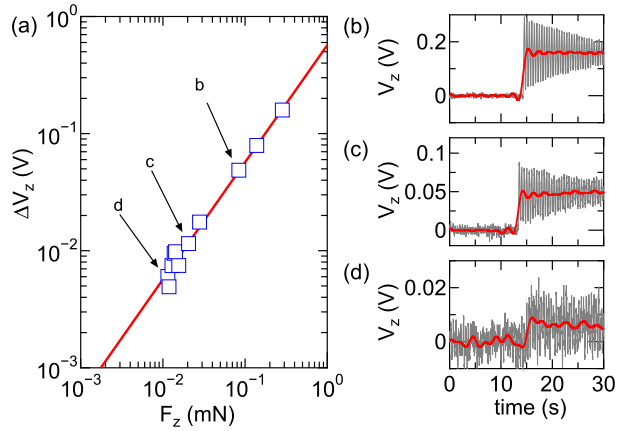

FIG. 7. (a) The axial displacement signal ΔV_z induced by turning on the dc calibration coil current I_{calz} as a function of the imparted force F_z, together with the calibration curve obtained from Fig. 4 and given by Eq. (7). The data obtained from (b-d) are labeled as 'b', 'c', and 'd', respectively. (b-d) Typical raw (thin lines) and filtered (bold lines) axial sensor signals V_z when turning on the dc current I_{calz} to the calibration coil, imparting the continuous axial forces of (b) ~ 85 μN, (c) ~ 20 μN, and (d) ~ 11 μN for $t > 15$ sec.

axial direction [Fig. 7(a)]. The sensor signal in the radial direction in Fig. 6(d) indicates no noticeable change of the displacement; hence it can be deduced that the lower limit of the radial force is about 20 μN. On the other hand, the clear change of the displacement signal [Figs. 7(b-d)] is observed for all the range of the force in the axial direction [Fig. 7(a)], implying the lower limit of the axial force detection of about 10 μN at least.

It should be mentioned that the rotational displacement, being approximated to the radial displacement, is actually induced by a torque rather than the radial force in the present MVMI structure. Considering the lengths L and L_0 of the arms having the detector and having the calibration coil, the radial forces $F_{\mathrm{det}\ r}$ to the detector can be obtained as

$$F_{det\ r} = \frac{L_0}{L} F_r. \tag{10}$$

When setting the arm length L at a few times the length L_0, the lower limit of the radial force detection less than $\sim$ 10 μN can be obtained.

IV. DISCUSSION

Figure 8 shows the axial profiles of the plasma density and the plasma potential in the helicon thruster operated in argon and with two solenoids powered with the equal solenoid current.[36] The center density is about 10^{12} cm^{-3} inside the source tube ($z < 0$) and $\sim$ 7 V potential drop is formed near the source center ($z \sim -10$ cm), contributing to the axial electrostatic ion acceleration. Under this condition, the axial force integrated over the inner surface of the source has been identified and shown the non-negligible loss of the axial momentum to the radial wall. Here the application of the presently developed MVMI to an investigation on the momentum loss to the radial wall in the helicon thruster is briefly discussed.

According to a low-pressure diffusion theory, the radial center-to-edge density ratio h_R is[37]

$$h_R = 0.8\left(4 + \frac{R}{\lambda_i}\right)^{-1/2}, \tag{11}$$

where R is the source tube radius in centimeters and $\lambda_i \sim (330 P_{Ar})^{-1}$ is the ion mean free path in centimeters for the argon pressure P_{Ar} in Torr; the sheath edge density is given as $n_s = h_R n_p$, where n_p is the density at the plasma center. Assuming a Maxwellian electron energy distribution giving an electron temperature T_e, the sum of the radial ion energies accelerated by the presheath voltage $-k_B T_e/e$ and by the sheath voltage $-k_B T_e/e \ \ln(m_i/2\pi m_e)$ is about $5.2 k_B T_e/e$, yielding the radial ion velocity u_r at the wall. Considering the typical values of the electron temperature of T_e = 6 eV, the density of $n_p = 1 \times 10^{12}$ cm^{-3}, the source radius of R = 3.5 cm, the gas pressure of 1 mTorr, the axial ion acceleration of 7 eV, the fluxes of the radial and axial momentums (corresponding to the force density) given by Eqs. (2) and (3) are $M_{dotr} \sim 1.2$ N $\cdot$ m^{-2} and $M_{dotz} \sim 0.6$ N $\cdot$ m^{-2}, respectively. Since the lower limits of the force detections are about 10 μN in both the radial and axial directions when taking Eq. (8) into account, the surface area of the detector has to be larger than

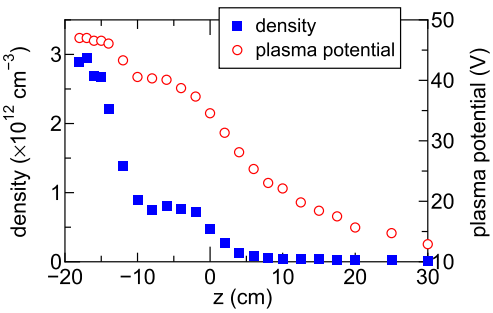

FIG. 8. Axial profile of the measured plasma density (filled squares) and the plasma potential (open circles) on axis in the previously reported 7-cm-diameter helicon thruster. Reproduced with permission from K. Takahashi and A. Ando, Plasma Phys. Control. Fusion **59**, 054007 (2017). Copyright 2017 IOP Publishing Ltd.

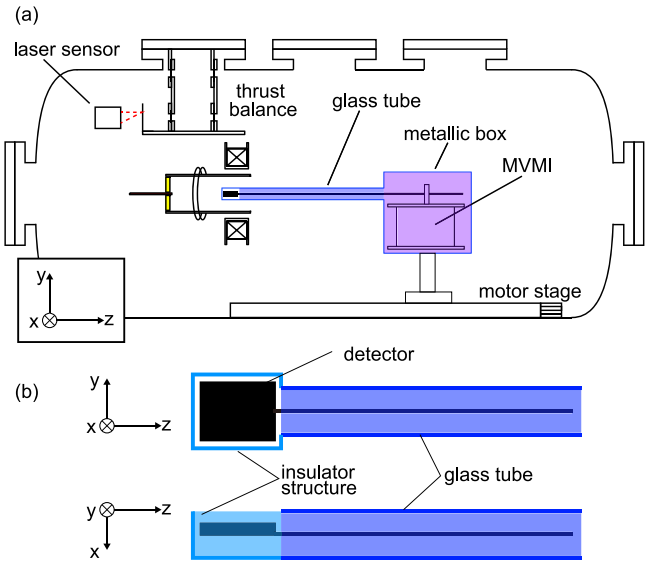

FIG. 9. (a) Schematic of the representative setup of the MVMI installation in a helicon thruster experiment. (b) The enlarged side and bottom views of the MVMI detector covered with the glass tube and the insulator structure, except for the one side surface of the detector plate.

$(10\ \mu\mathrm{N})/(0.6\ \mathrm{N}\cdot\mathrm{m}^{-2}) \sim 0.17\ \mathrm{cm}^2$ at least for the considered condition. Therefore, the detector having the surface of a few cm^2 will detect the fluxes of both the radial and axial momentums.

Figure 9(a) shows a representative setup of the MVMI installation, which is planned in future experiment, and Fig. 9(b) shows the enlarged side and bottom views of the MVMI detector. The whole structure of the MVMI, except for one side of the detector surface, is covered with a metallic box, a glass tube, and an insulator structure as painted out in Fig. 9, where the long arm covered with the glass and the insulator allows the detector to be inserted into the source tube. By mounting the structure to the axially movable motor stage and setting the sensor near the radial wall, axial profiles of the radial and axial momentums lost to the wall will be obtained in future experiment.

The thermal stress to the MVMI and the resultantly occurring displacement signal would also be inhibited by covering the MVMI as in Fig. 9. Since the previous experiment in Ref. 35 has shown that the force to the large target plate (same material as the present experiment) is in good agreement with the thrust directly measured by the thrust balance, the mass ejection from the target material and the ion reflection at the detector surface are considered not to affect the force measurement accuracy. However, inserting the MVMI detector into the source tube might disturb the plasma and the dynamics of the charged particles near the detector surface would be very complicated due to a disturbed electric field near the detector edge. Furthermore mechanical vibration coming from the vacuum pumping system and the force due to the presence of the magnetic and electric fields possibly affect the stability and accuracy of the MVMI. Therefore combination of the MVMI and the thrust balance (as in Fig. 9) or the plasma diagnosis such as an Langmuir probe will be useful to clarify the momentum transport in the helicon thruster, which still remains future challenge.

As described above, the results in the helicon thruster is not shown in the present paper. However the MVMI providing the high resolution, vector-resolved, and spatially-resolved measurement of the momentum flux can potentially be used not only in the helicon thruster but also in many fundamental experiments, e.g., plasma-wall interaction and divertor plasmas simulating a fusion reactor,[38] the assessment of divergences of the ion and neutral beams,[39] and so on, where the absolute plasma diagnosis at the solid surface is often difficult to perform.

V. CONCLUSION

The momentum vector measurement instruments (MVMI) having the structure accessible to the inside of the thruster is developed and its bench test is performed here; demonstrating the simultaneous

and individual measurements of the radial and axial forces to the detector surface, i.e., the fluxes of the radial and axial momentums. The bench test shows that the small force close to 10 μN is detectable for both the radial and axial directions, resulting in the application to the spatially-resolved measurement of the momentum loss inside the helicon plasma thruster.

ACKNOWLEDGMENTS

This work is partially supported by JSPS KAKENHI Grant No. 16H04084, 18K18746, and 18K18907, Research Foundation for the Electrotechnology of Chubu, and JAXA.

[1] A. Fruchtman, Phys. Rev. Lett. **96**, 065002 (2006).
[2] E. Ahedo and M. Merino, Phys. Plasmas **17**, 073501 (2010).
[3] A. Fruchtman, K. Takahashi, C. Charles, and R. W. Boswell, Phys. Plasmas **19**, 033507 (2012).
[4] K. Takahashi, T. Lafleur, C. Charles, P. Alexander, and R. W. Boswell, Phys. Plasmas **19**, 083509 (2012).
[5] T. E. Sheridan, Phys. Plasmas **7**, 3084 (2000).
[6] D. Lee and N. Hershkowitz, Phys. Plasmas **14**, 033507 (2007).
[7] U. Kortshagen, I. Pukropski, and M. Zethoff, J. Appl. Phys. **76**, 2048 (1994).
[8] V. A. Godyak, R. B. Piejak, and B. M. Alexandrovich, Plasma Sources Sci. Technol. **11**, 525 (2002).
[9] K. Takahashi, C. Charles, R. W. Boswell, T. Kaneko, and R. Hatakeyama, Phys. Plasmas **14**, 114503 (2007).
[10] K. Takahashi, C. Charles, R. W. Boswell, and T. Fujiwara, Phys. Rev. Lett. **107**, 035002 (2011).
[11] R. Hardin, X. Sun, and E. E. Scime, Rev. Sci. Instrum. **75**, 4103 (2004).
[12] X. Sun, A. M. Keesee, C. Biloiu, and E. E. Scime, Phys. Rev. Lett. **95**, 025004 (2005).
[13] M. Aramaki, K. Ogiwara, S. Etoh, S. Yoshimura, and M. Y. Tanaka, Rev. Sci. Instrum. **80**, 053505 (2009).
[14] K. G. Xu and M. L. R. Walker, Rev. Sci. Instrum. **80**, 055103 (2009).
[15] S. Pottinger, V. Lappas, C. Charles, and R. Boswell, J. Phys. D: Appl. Phys. **44**, 235201 (2011).
[16] K. Takahashi, T. Lafleur, C. Charles, P. Alexander, R. W. Boswell, M. Perren, R. Laine, S. Pottinger, V. Lappas, T. Harle, and D. Lamprou, Appl. Phys. Lett. **98**, 141503 (2011).
[17] A. Shabshelowitz and A. D. Gallimore, J. Propul. Power **30**, 664 (2014).
[18] R. Yanagi and I. Kimura, J. Spacecr. Rockets **19**, 246 (1982).
[19] D. G. Chavers and F. R. Chang-Díaz, Rev. Sci. Instrum. **73**, 3500 (2002).
[20] B. W. Longmier, B. M. Reid, A. D. Gallimore, F. R. Chang-Díaz, J. P. Squire, T. W. Glover, G. Chavers, and E. A. Bering III, J. Propul. Power **25**, 746 (2009).
[21] K. Takahashi, T. Lafleur, C. Charles, P. Alexander, and R. W. Boswell, Phys. Rev. Lett. **107**, 235001 (2011).
[22] K. Takahashi, C. Charles, and R. W. Boswell, Phys. Rev. Lett. **110**, 195003 (2013).
[23] K. Takahashi, A. Chiba, A. Komuro, and A. Ando, Phys. Rev. Lett. **114**, 195001 (2015).
[24] K. Takahashi, H. Akahoshi, C. Charles, R. W. Boswell, and A. Ando, Phys. Plasmas **24**, 084503 (2017).
[25] A. Fruchtman, G. Makrinich, P. Chabert, and J. M. Rax, Phys. Rev. Lett. **95**, 115002 (2005).
[26] A. Fruchtman, IEEE Trans, Plasma Sci. **36**, 403 (2008).
[27] K. Takahashi, Y. Takao, and A. Ando, Appl. Phys. Lett. **108**, 074103 (2016).
[28] K. Takahashi, Y. Takao, and A. Ando, Appl. Phys. Lett. **109**, 194191 (2016).
[29] Y. Takao and K. Takahashi, Phys. Plasmas **22**, 113509 (2015).
[30] K. Takase, K. Takahashi, and Y. Takao, Phys. Plasmas **25**, 023507 (2018).
[31] T. Lafleur, Phys. Plasmas **21**, 043507 (2014).
[32] N. Nagao, S. Yokota, K. Komurasaki, and Y. Arakawa, Rev. Sci. Instrum. **78**, 115108 (2007).
[33] A. Spethmann, T. Trottenberg, H. Kersten, F. G. Hey, L. Grimaud, and S. Mazouffre, Proceedings of the 35th International Electric Propulsion Conference, Atlanta, Georgia, USA, IEPC-2017-245 (2017).
[34] A. Spethmann, T. Trottenberg, and H. Kersten, Phys. Plasmas **24**, 093501 (2017).
[35] K. Takahashi, A. Komuro, and A. Ando, Rev. Sci. Instrum. **86**, 023505 (2015).
[36] K. Takahashi and A. Ando, Plasma Phys. Control. Fusion **59**, 054007 (2017).
[37] M. A. Lieberman and A. J. Lichtenberg, *Principles of Plasma Discharges and Materials Processing*, 2nd ed. (John Wiley & Sons, New Jersey, 2005).
[38] N. Ohno, D. Nishijima, S. Takamura, Y. Uesugi, M. Motoyama, N. Hattori, H. Arakawa, N. Ezumi, S. Krasheninnikov, A. Pigarov, and U. Wenzel, Nucl. Fusion **41**, 1055 (2001).
[39] K. Tsumori, M. Osakabe, Y. Takeiri, O. Kaneko, K. Nagaoka, K. Ikeda, H. Nakano, Y. Oka, M. Shibuya, E. Asano, S. Komada, T. Kondo, and M. Sato, Rev. Sci. Instrum. **81**, 02B117 (2010).